Research Article

Study on the Upper Limit of Roof Failure in Soft Rock Roadway

Jie Zhang,[1,2] **Shoushi Gao** ⬤,[1] **Yifeng He,**[1] **Tao Yang,**[1] **Tong Li,**[3] **Yihui Yan,**[1] **and Jianping Sun**[1]

[1]*School of Energy Resources, Xi'an University of Science and Technology, Xian 710054, China*
[2]*Key Laboratory of Mine Mining and Disaster Prevention in West China, Ministry of Education, Xian 710054, China*
[3]*China Coal Xi'an Design Engineering Co., Ltd., Xian 710054, China*

Correspondence should be addressed to Shoushi Gao; gaoshoushi8@163.com

This study addresses the issue of large deformation in soft rock roadways, using the 50213 tailgate of Guantun Coal Mine as a case study. Field investigations were conducted to assess the condition of roadway bolts, anchor cables, and the internal damage characteristics of the surrounding rock. The upper bound method of limit analysis in plastic mechanics was utilized to construct a failure model for the surrounding rock and derive the upper limit solution of roof failure by integrating the principle of virtual work and variational extremum theorem. Physical similarity simulations were employed to investigate the fracture distribution and evolution law of the surrounding rock. Based on the deformation and instability mechanism of the roadway, optimized support parameters for soft rock roadways were proposed and verified through numerical simulation. The results indicate that the surrounding rock of the sharp corner of the roadway is initially destroyed and develops upward with increasing stress. The interconnected horizontal separation cracks at the anchorage end of the anchor cable and shear fracture zones at the two corners ultimately lead to the overall instability of the anchorage arch. Furthermore, the theoretical calculation boundary exhibited significant similarity with the failure evolution law and distribution pattern. Following the adoption of the optimized support scheme, roof subsidence decreased by 46.7% compared to the original scheme, and the amount of movement on both sides decreased by 36.2%. The control effect of the surrounding rock was favorable, and its internal stability was significantly improved, thereby effectively resolving the issue of large deformation in soft rock roadways.

1. Introduction

Due to the depletion of coal resources in central and eastern China, there has been a gradual shift of coal mining activities towards northwest China, particularly in regions such as Xinjiang, Shaanxi, and Ningxia, where engineered soft rock strata are prevalent [1, 2]. These rock formations are commonly characterized by weak cementation, high clay mineral content, and a propensity to swell and soften upon exposure to water. Excavation within these formations is susceptible to disasters such as roof caving, rib spalling, and potential collapse. Hence, the study of the mechanism behind soft rock roadway roof falls holds significant practical importance in effectively preventing accidents and ensuring the implementation of safe coal mining practices.

The damage process of soft rock roadways has been the subject of extensive research by scholars in China and abroad, yielding significant insights. Huang [3–5] simplified the roadway roof into a beam model, enabling the calculation of stress distribution and deformation characteristics. Chen et al. [6, 7] developed models for roadway roofs of varying thicknesses, by employing the elastoplastic theory to determine the failure modes of these roofs. Liu et al. [8–10] utilized numerical simulation techniques to establish a computational model, facilitating the study of stress variation and fracture mechanisms in roadway roofs. Jia et al. [11, 12] used FLAC^{3D} numerical simulation software to investigate roadway roofs containing coal seams of different thicknesses with low strength, identifying the primary causes of severe deformation of soft rock roadways. Li et al. [13–16] determined the distribution pattern of the plastic zone of the

surrounding rock of the roadway through theoretical analysis. In response to the failure characteristics of soft rock roadways, Zhao et al. [17–20] examined the deformation mechanism of deep roadways and proposed a composite support technology for the surrounding rock. Fraldi and Guarracino [21–25] incorporated the limit analysis method of plastic mechanics into the computational analysis of soft rock roadway roof stability, revealing the destabilization damage mechanism from an energy dissipation perspective. Finally, Li et al. [26–31] established a mechanical model of the coal wall. Using the deflection theory for material mechanics, they identified the maximum deflection point of the coal wall, which is most prone to deformation and damage during mining, based on the mining conditions of the 12–2 up 108 working face in the Jinjitan Coal Mine.

The limit analysis upper bound method is employed to address the issue of soft rock roof fall damage. This is achieved by establishing a model for roadway roof damage and the velocity field of motion, utilizing the principle of equilibrium between work and energy conversion processes. This methodology simplifies the intricate issue of soft rock roof fall damage, circumventing laborious calculations, thereby presenting a novel approach for investigating the mechanisms of soft rock roof collapse. Utilizing the limit analysis method, this study takes into account various factors, including the stress of the surrounding rock and the load supported by the roadway roof, to derive a formula for calculating the failure height of the roadway roof. This provides a precise theoretical reference for designing the support characteristics of surrounding rocks in soft rock roadways.

2. Engineering Background

2.1. Project Overview. The 50213 panel of the Guantun Coal Mine features an average burial depth of 204 m. The average thickness of the coal seam is 2.12 m, with an inclination ranging from 0 to 4°. The panel is bordered by the auxiliary transport roadway to the south, the 50212 gob to the east, the 50214 panels to the west, and the mining area boundary to the north. Figure 1 depicts the histogram of the coal and rock seams at the working face.

The main roof of the panel comprises 10.12 m of fine-grained sandstone, characterized as semihard rock. The immediate roof consists of 1.28 m of siltstone followed by 5.95 m of oil shale. The siltstone layer is rich in clay minerals and organic matter, with well-developed structural surfaces including joints, fissures, and slip surfaces. The oil shale layer predominantly exhibits horizontal bedding and minor cross-bedding. Upon prolonged immersion in water or exposure to air, it disintegrates into slices along the bedding direction. The saturated strength of compression is 14.9 MPa and the softening index is 0.6. The immediate floor is composed of a 2.0 m thick layer of mudstone. The mudstone has a saturated compressive strength of 10.1 MPa, exhibits significant expansion when exposed to water, and has a softening coefficient of 0.59.

The 50213 tailgate is a semicoal rock roadway, excavated along the roof of the coal seam, spanning a total length of 1400 m. The tailgate features a rectangular cross-section,

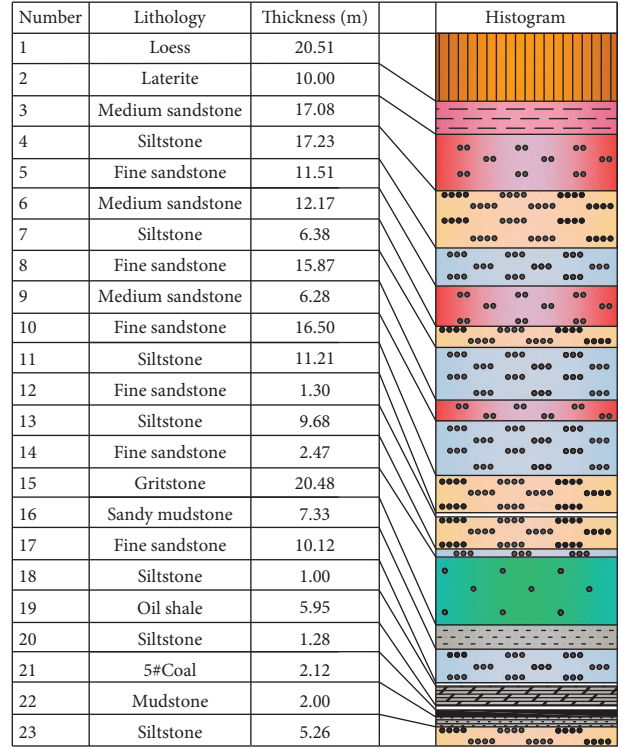| Number	Lithology	Thickness (m)	Histogram
1	Loess	20.51	
2	Laterite	10.00	
3	Medium sandstone	17.08	
4	Siltstone	17.23	
5	Fine sandstone	11.51	
6	Medium sandstone	12.17	
7	Siltstone	6.38	
8	Fine sandstone	15.87	
9	Medium sandstone	6.28	
10	Fine sandstone	16.50	
11	Siltstone	11.21	
12	Fine sandstone	1.30	
13	Siltstone	9.68	
14	Fine sandstone	2.47	
15	Gritstone	20.48	
16	Sandy mudstone	7.33	
17	Fine sandstone	10.12	
18	Siltstone	1.00	
19	Oil shale	5.95	
20	Siltstone	1.28	
21	5#Coal	2.12	
22	Mudstone	2.00	
23	Siltstone	5.26	

Figure 1: Coal seam and rock stratum histogram.

measuring 4200 mm in width and 2800 mm in height. The support system employed is a bolt-mesh-cable structure. The roof is reinforced using steel bolts, each with a diameter of 22 mm and a length of 2400 mm. These bolts are arranged in a grid pattern with a spacing of 900 mm × 900 mm. On both sides of the roadway, left-handed thread steel bolts are used. These bolts have a diameter of 20 mm and a length of 2200 mm and are arranged with a row spacing of 1100 mm × 900 mm. The steel strand anchor cable, used in the support structure, measures 7200 mm in length and 18.9 mm in diameter, with a spacing of 900 mm. Figure 2 provides a schematic diagram of the roadway support.

2.2. Field Investigation and Research

2.2.1. Bolt and Cable Load Detection. In order to analyze temporal changes in the bolt and anchor cable load of the 50213 tailgate, and to subsequently facilitate the optimization of support parameters, we conducted tests on the bolt and anchor cable load using a dynamometer. The specific locations of the monitoring stations and measuring points are shown in Figure 3. The testing area comprised four measuring stations, each equipped with an anchor cable measuring point, in addition to bolt measuring points located at the roof and on both sides. Figure 4 shows the changing curve of the bolt and the anchor cable load. Observations made when the measurement station was positioned at 200 m from the excavation face revealed that the maximal axial force of the side bolt was 103 kN (bolt B_2 of measuring station T_1), while its minimal axial force was 75 kN (bolt B_2 of measuring station T_3). The average axial
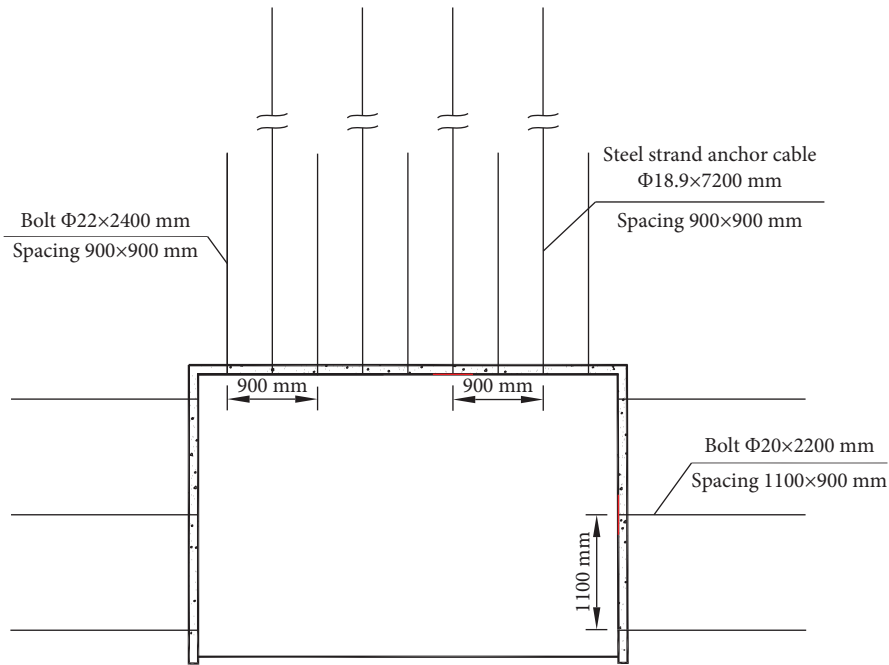
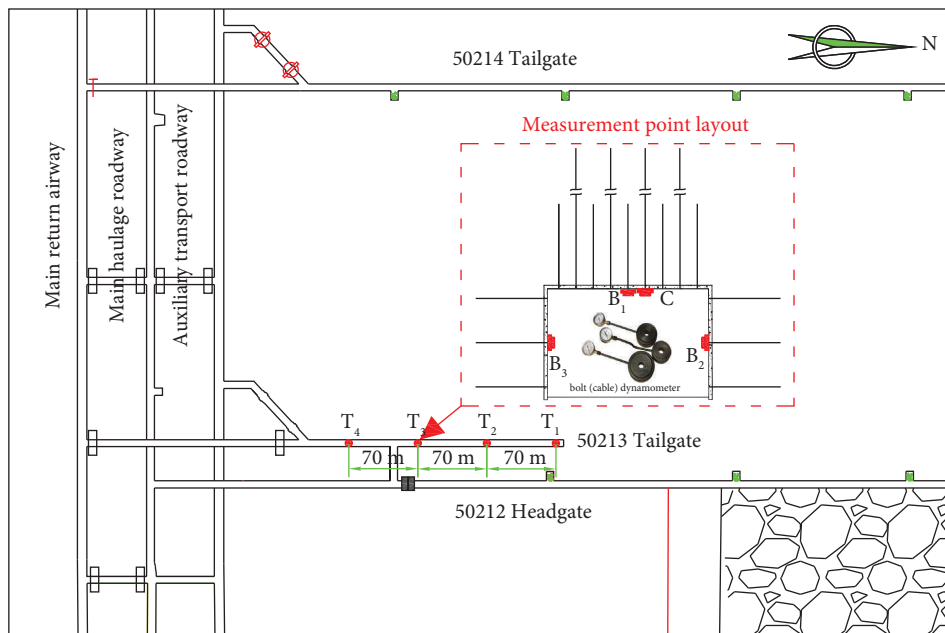FIGURE 2: Roadway support layout diagram.

FIGURE 3: Bolt and anchor cable station layout plan.

forces at measurement points B_2 and B_3 were 91.5 kN and 90.5 kN. The axial load of the rib side was found to be considerable, with some measurements exceeding the anchorage force limit specified in the design.

At a distance of 200 m from the excavation working face, the axial stress of the roadway roof bolt varied. The maximum recorded stress was 112 kN (observed in bolt B_1 at measuring station T_3), while the minimum was 78 kN (observed in bolt B_1 at measuring station T_1). The average axial force was calculated to be 94.7 kN. The axial stress of the anchor cable also showed variation. The maximum stress recorded was 161 kN (at the measurement station T_1), and the minimum was 147 kN (at the measurement station T_3). The average axial force for the anchor cable was determined to be 152.7 kN. The monitoring data indicated that the axial force for both the bolt and anchor cable was substantial.
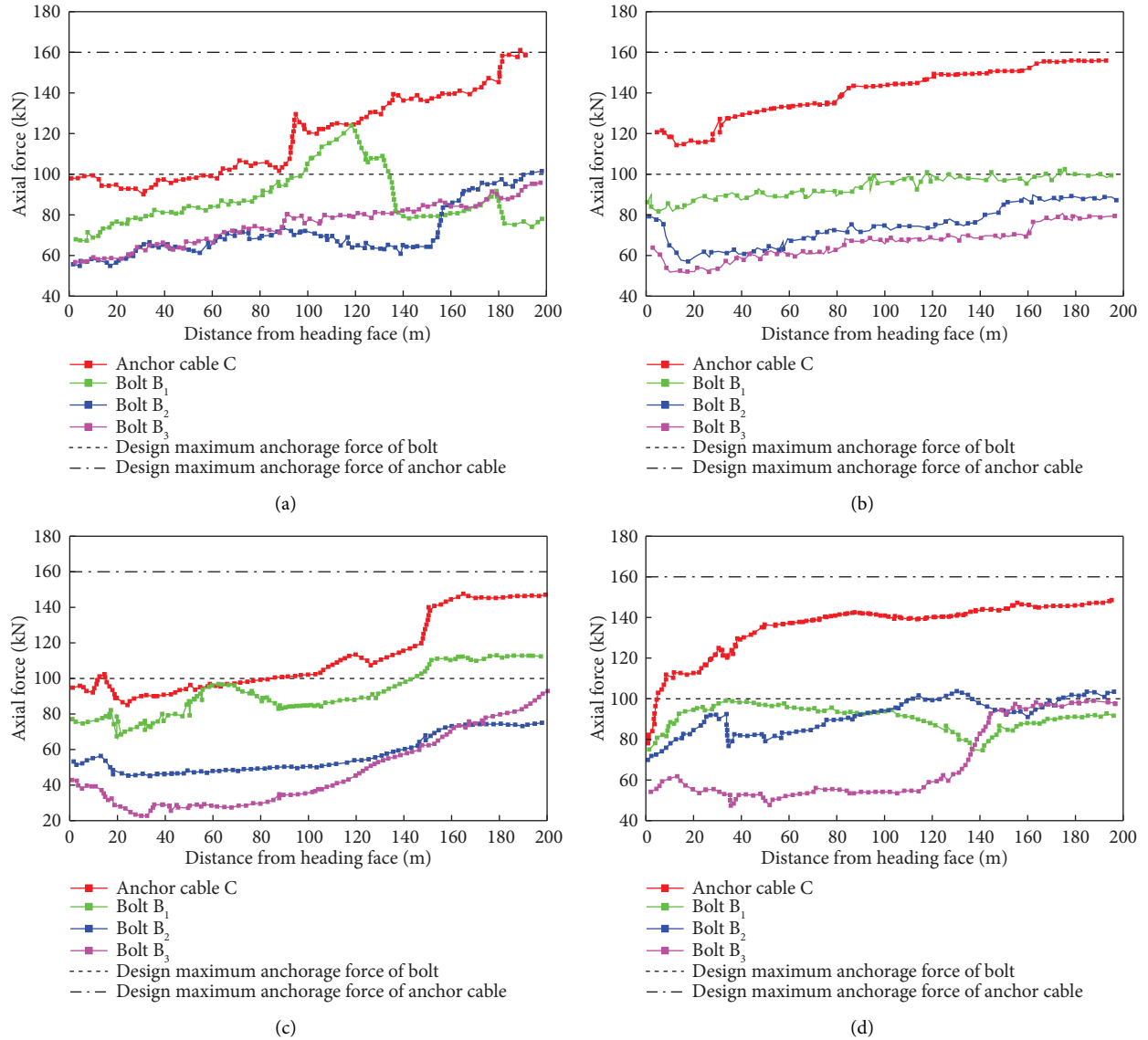
Figure 4: Axial force variation curve of bolt and cable. (a) Measuring station T_1. (b) Measuring station T_2. (c) Measuring station T_3. (d) Measuring station T_4.

Notably, the axial force of several bolts exceeded the maximum design value for anchorage force. This force then decreased rapidly, leading to a reduction in bolt working resistance.

2.2.2. Internal Damage Characteristics of Roadway Surrounding Rock. Drilling holes are excavated for the purpose of observing fissures in the roof and on both sides of the tailgate, with a depth of 10.0 m in the roof and 5 m on the two sides. The CXK-12 borehole video recorder was utilized to conduct a quantitative analysis of the internal crack damage features and the extent of damage to the roadway surrounding the rock. The characteristics of the damage to the various layers of rock are illustrated in Figure 5.

The borehole observation results indicate that the superficial part of the roadway roof, specifically the first 1.13 meters, contains broken and loose rocks. From a depth of 2.0 m to 5.5 m, several longitudinal cracks ranging from 1 mm to 2 mm in width are present. The number of separation cracks within the borehole increases significantly between the depths of 6.9 m and 7.5 m. However, as the drilling depth increases, the surrounding rock's integrity begins to improve and the degree of fragmentation decreases. When the drilling depth reaches between 7.5 m and 10.0 m, the rock layer of the borehole wall appears smooth and complete. The borehole maintains a round shape, and the rock layers exhibit good stability. On the left side, a small portion of the area is broken within the depth range of 0 m–0.4 m, and a few longitudinal fissures are present between 1.0 m and 1.85 m. On the right side, the breakage is more severe from 0 m to 0.95 m, and a few longitudinal cracks are present between 1.4 m and 2.2 m.
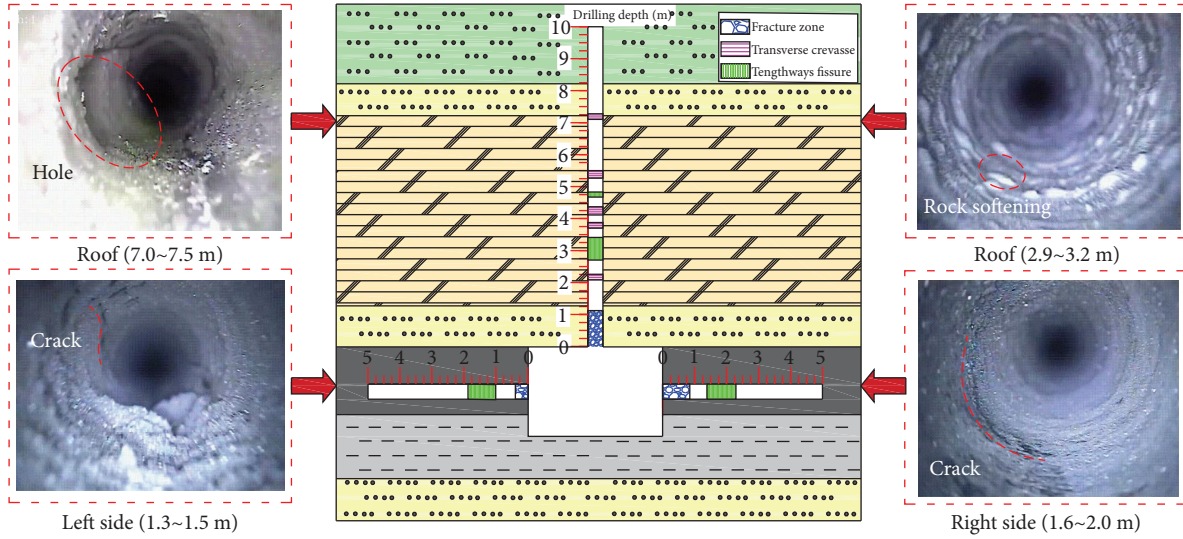
FIGURE 5: Fracture distribution characteristics of the surrounding rock.

3. Calculation of Failure Height of Soft Rock Roadway Roof Based on the Limit Analysis Method

3.1. Basic Assumptions

(1) Assuming the tunnel axis as infinitely long allows us to simplify the analysis to a two-dimensional plane strain problem.

(2) The rock mass, adhering to the relevant flow equation, behaves as an ideal plastic material.

(3) During failure, the volume remains constant, treating the slider as a rigid block. In the case of zero volume strain, energy loss is experienced solely by the velocity discontinuity line.

(4) For the purposes of this analysis, the energy dissipation rate within the slider is considered negligible.

3.2. Limit Analysis Upper Bound Method.

This approach is proposed based on the principle of virtual work and the variational extremum theorem. An assumed failure mode is necessary prior to determining the upper bound solution. We assume that the internal energy dissipation rate along the velocity discontinuity line is greater than or equal to the power exerted by the external force on the rigid block, as expressed by the following equation. The limiting failure height, crucial for maintaining roadway stability, can be determined through continuous adjustment of the strength parameters. Furthermore, this approach can be utilized to evaluate roadway stability and provide recommendations for optimal supporting parameters.

$$\int_V \sigma_{ij}\varepsilon_{ij}dV \geq \int_S T_i v_i ds + \int_V X_i v_i dV, \tag{1}$$

where σ_{ij} and ε_{ij} are the stress tensor and strain tensor in the velocity field, respectively, T_i is the surface force vector acting on the boundary S, X_i is the body force vector acting in the region V, and v_i is the vector on the speed discontinuities curve.

3.3. Failure Model of Soft Rock Roadway Surrounding Rock.

This paper constructs a failure model for the roadway surrounding rock and the speed vector of movement, drawing upon the methodologies presented in the studies by Yang and Yang [32–36]. Considerations are given to factors such as the support load and the load of the overburdened rock. Furthermore, an energy consumption analysis is conducted. The failure model of the soft rock roadway is shown in Figure 6. Postexcavation, the roadway is influenced by the gravity of the rock mass and the stress exerted by the strata above, resulting in the formation of the fracture surface ECABDF. The velocity of the quadrilateral slider ACDB is v_0, the velocity of the discontinuities CM and DN is v_{01}, and the velocity of the triangular sliders CEM and DFN is v_1. Within the velocity field of motion, v_0, v_{01}, and v_1 adhere to the vector closure relation, specifically, $v_0 + v_{01} = v_1$. When the roadway reaches the limit failure state, the applied support strength equals the pressure exerted by the surrounding rock.

The length of each velocity discontinuity line in Figure 6(a) can be calculated from the following formula:

$$AC = \frac{H}{\cos\varphi_t},$$

$$CM = h\tan\alpha,$$

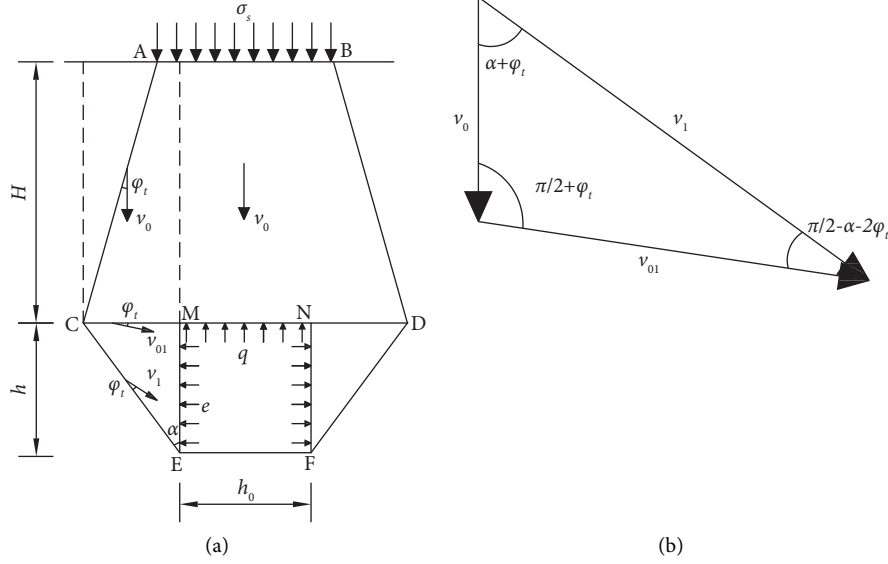$$CE = \frac{h}{\cos\alpha}, \tag{2}$$

$$AB = 2CM + h_0 - 2H\tan\varphi_t,$$

FIGURE 6: Failure model of soft rock roadway. (a) Damage model. (b) Velocity vector.

where H represents the failure height of the roadway roof, m; h is the height of the roadway, m; h_0 is the width of the roadway, m; φ_t is the angle between the velocity vector and its corresponding fracture surface, °; which is equal to the internal friction angle of rock mass; and α is the fracture angle, °.

The following formula can be used to determine the area of each slider:

$$S_0 = S_{ACDB} = H\left(2h_0 + 4h\tan\alpha - 2H\tan\varphi_t\right),$$

$$S_1 = S_{CEM} = \frac{1}{2}h^2\tan\alpha. \tag{3}$$

According to the velocity vector relationship in Figure 6(b), we have

$$\begin{cases} v_1 = \dfrac{\sin\left(\pi/2 + \varphi_t\right)}{\sin\left(\pi/2 - \alpha - 2\varphi_t\right)}v_0, \\[4mm] v_{01} = \dfrac{\sin\left(\alpha + \varphi_t\right)}{\sin\left(\pi/2 - \alpha - 2\varphi_t\right)}v_0. \end{cases} \tag{4}$$

3.4. Energy Consumption Analysis of Roadway Surrounding Rock. The gravitational force acting on the sliders ACDB, CEM, and DFN can be expressed as the algebraic sum of the product of each slider's gravitational force and its velocity. The mathematical expression for this can be formulated as follows:

$$P_\gamma = \gamma S_0 v_0 + 2\gamma S_1 v_1 \cos\left(\alpha + \varphi_t\right). \tag{5}$$

The power made by the support force is equal to the product of the support force and its speed, and its expression is as follows:

$$P_T = -qh_0 v_0 - 2ehv_1\cos\left(\frac{\pi}{2} - \alpha - \varphi_t\right), \tag{6}$$

where q and e are the support force of the roadway roof and roadway rib sides, respectively, e = Kq, and K is the lateral pressure coefficient.

The power produced by the overburden load σ_s is equal to the product of overburden load and its velocity, which is expressed as follows:

$$P_s = \sigma_s v_0 \left(2h\tan\alpha + h_0 - 2H\tan\varphi_t\right). \tag{7}$$

In this formula, σ_s is the load of overlying strata, MPa.

The internal energy dissipation occurs only on the velocity discontinuity line during roadway failure. Then, the internal energy dissipation rate is equal to the product of the cohesive force of rock mass on the velocity discontinuity line and its velocity. The expression is as follows:

$$P_V = c_t \cos\varphi_t \left(ABv_0 + 2ACv_0 + 2CMv_{01} + 2CEv_1\right). \tag{8}$$

3.5. Upper Bound Solution of Failure Height of Roadway Roof. The failure model developed demonstrates that the externally applied power and internal heat removal power are equivalent, in accordance with the upper bound theorem of limit analysis, as expressed in the following equation:

$$P_\gamma + P_T + P_s = P_V. \tag{9}$$

By substituting formulas (5)–(8) into equation (9), the upper limit objective function of the damage height of the roadway roof can be obtained as follows:

$$H = f\left(\gamma, \alpha, \varphi_t, \sigma_s, c_t, h_0, h, K, q\right). \tag{10}$$

The constraint condition in solving the height of damage to the roof of the roadway is as follows:

$$\begin{cases} \alpha + \varphi_t > 0, \\ \pi/2 - \alpha - 2\varphi_t > 0. \end{cases} \tag{11}$$

The failure height H of the roof of the roadway is a function of the overburden density γ, the fracture angle α, the internal friction angle φ_t, the load σ_s of the surface layers, the cohesion c_t of the surrounding rock, the width h_0, the height h, the pressure coefficient K, and the support strength q. Collectively, these factors determine the damage height of the roadway. Therefore, the most unstable fracture surface of the roadway can be obtained by solving the maximum value of the objective function H under the constraint condition.

Due to the presence of multiple nonlinearly related variables in equation (10), analytical solutions are not readily attainable. As a result, this paper employs MATLAB to solve the objective function (10) under multivariate constraints, ultimately obtaining the maximum value within the local area. This approach yields the upper limit solution for the damage height of the roadway roof.

4. Calculation of the Failure Height of the Roadway Roof and Verification of the Damage Model

4.1. Calculation of the Damage Height of the Roof of the Roadway.
Using the 50213 working face tailgate of the Guantun Coal Mine as the technical background, the height of roof failure under different overlying strata loads was calculated based on the upper limit objective function calculation formula of equation (10). Table 1 shows a list of the pertinent characteristics of the tailgate's surrounding rock.

Based on the technical context of the 50213 tailgate at the Guantun Coal Mine, an analysis was conducted to calculate the roof failure height under varying overlying strata loads using the objective function calculation formula equation (10). Table 1 presents the relevant parameters of the surrounding rock of the tailgate.

Based on the analysis conducted using MATLAB, the curve depicting the variation in failure height of the tailgate roof under varying overlying loads is presented in Figure 7. The graphical representation illustrates a nonlinear increase in the upper limit of roadway roof failure height with the escalation of overburden load.

4.2. Verification of the Roadway Surrounding Rock Failure Model and Roof Failure Height

4.2.1. Experimental Design.
For the load testing, we utilized a model frame with dimensions of 2.1 m in length and 1.8 m in height. The primary objective of the test is to simulate the failure mechanism of the 50213 tailgate. The simulated material comprises river sand as the aggregate and a mixture of calcium carbonate and gypsum as the cementing material. These materials are mixed with water in accordance with the proportioning numbers in Table 2. Mica powder is employed as the layering material. According to the similarity theory of the simulation experiment, the geometric similarity constant was chosen as 10, the bulk density similarity constant was chosen as 1.6, and the strength similarity constant was chosen as 16. The actual photo of the model is shown in Figure 8.

Based on the similarity ratio and the parameters of the original bolt and anchor cable, we calculated the geometric, physical, and mechanical parameters for the bolt and anchor cable in the physical simulation model. We conducted a pull-out test on the bolt and anchor cable simulation materials using a laboratory pull-out test machine. The selection of appropriate simulation materials for the bolt and anchor cable was based on the breaking load and similarity ratio. We concluded that the simulated roof bolt should be an aluminum wire with a diameter of 2.2 mm and a length of 240 mm, the side bolt should be an aluminum wire with a diameter of 2.0 mm and a length of 220 mm, and the anchor cable should be an iron wire with a diameter of 1.89 mm and a length of 720 mm. The parameters of the bolt and anchor cable are listed in Table 3.

In order to facilitate the analysis of the failure characteristics and evolution process of the surrounding rock of the roadway, we implemented a step-by-step loading test. The actual surrounding rock stress in the tailgate of the 50213 panel is 7.7 MPa. According to the stress similarity constant 16, the surrounding rock stress applied to the model lane is 0.481 MPa. Since the model size is 2.1 m in length and 0.4 m in width, the load applied to the upper layer of the model is 393.1 kN. The loading is carried out step by step, and the loading steps are designed as 10 steps (step 1~step 10). The magnitude of the applied horizontal load is obtained by using the following equation, and the step-by-step loading scheme of the test model is listed in Table 4.

$$q_2 = q_1 \times K, \tag{12}$$

where q_2 is the horizontal load of the model, N; q_1 is the vertical loading load of the model, N; and K is the lateral pressure coefficient, which is taken as 0.12.

4.2.2. Fracture Evolution Law of Surrounding Rock

(1) Fracture Distribution in the Slow Deformation Stage. The roof undergoes bending and sinking as the confining pressure is progressively applied from step 1 to step 6. Longitudinal cracks emerge at the two sharp corners of the roadway, a result of the concentration of shear stress. Simultaneously, as each layer of the immediate roof experiences different deflection during sinking, it becomes conducive to the formation of horizontal separation cracks along the layers. The intersection of horizontal and longitudinal fissures culminates in the formation of two sharp-cornered fissure zones.

Second, the concentration of stress is propagated to the two lower corners via the two lateral sides. Owing to the poor mechanical properties of the floor and insufficient support, a shear failure zone is readily formed at the two lower corners. The pattern of fracture distribution aligns with the model pattern derived from theoretical calculations. The model indicates a roof damage height of 1.2 m, while the theoretical calculation suggests a damage height of 1.14 m, as depicted in Figure 9.

TABLE 1: Related parameters of the surrounding rock of tailgate.

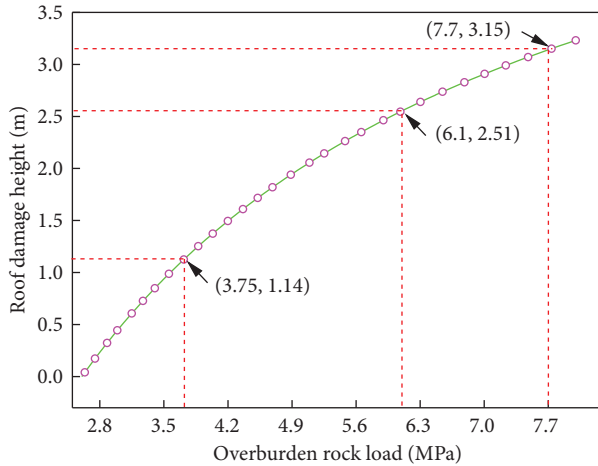| Fracture angle (°)	Internal friction angle (°)	Cohesion (MPa)	Overburden density (N·m⁻³)	Width of the roadway (m)	Height of the roadway (m)	Pressure coefficient	Support strength (MPa)
28	34	1.08	25470	4.2	2.8	1	0.2

FIGURE 7: Variation law of failure height of tailgate roof.

(2) Fracture Distribution in the Rapid Deformation Stage. During the process where confining pressure is applied, specifically from step 6 to step 9, the anchor cable anchorage zone, primarily composed of a thick, low-strength oil shale layer, experiences an increase in the width of the fissures located at the two sharp corners. This continues to extend upward, resulting in the formation of a "truncated cone" block in the roof above the roadway. The uncoordinated deformation and movement between the inner and outer rock layers of the "truncated cone" lead to the appearance of horizontal bed separation cracks at the end of the anchor cable.

The sidewall fissure extends diagonally upward at an angle of 65° from the bottom corner of the roadway. The coal in the shallow part is fragmented and exhibits poor stability. The maximum damage depth is 1.9 m. Tensile and bed separation cracks are generated during the bending and deformation of the floor to the free surface. The fracture distribution pattern obtained from a simulation mirroring the mine conditions is consistent with the pattern derived from the theoretical calculation based on geological data. The damage height of the roof, as determined from the model simulation, is 3.1 m, while the damage height derived from the theoretical calculation is 2.51 m, as shown in Figure 10.

(3) Fracture Distribution in the Sharp Deformation Stage. Upon increasing the confining pressure from step 9 to step 10, the distribution range of cracks attains its maximum. The sharp corner fractures intersect with the horizontal bed-separated crack at the end of the anchor cable. The subsidence rate of the rock strata within the "truncated cone" region accelerates. The dimensions, specifically the width and length, of the two bed-separated fissures at the end of the anchor cable increase. The rock strata within a 1.2 m vertical range from the floor exhibit damage and upward bulging. The model simulation suggests a roof damage height of 3.1 m, while the theoretical calculation indicates a slightly higher value of 3.15 m, as depicted in Figure 11.

During the occurrence of roadway damage, the surrounding rock encompasses both plastic and elastic deformation zones. The demarcation between the elastic and plastic zones is characterized by a velocity discontinuity line. Upon the destruction of the surrounding rock, the discontinuity line manifests as a series of longitudinal cracks. The velocity discontinuity line, derived from theoretical calculations, is compared with the fracture distribution of the surrounding rock, as obtained from analogous simulations. The fracture distribution is found to be consistent across both sides. Despite the varying development heights of the roadway roof fissures, their distribution and evolutionary patterns exhibit notable similarities. Consequently, the aforementioned theory is applicable in studying the failure evolution law of the soft rock constituting the roadway's surrounding rock.

4.2.3. Analysis of Roadway Surface Displacement Monitoring Results. As depicted in Figure 8, measurement points no. 1–3 are positioned from the bottom to the top on the left side of the road, while points no. 4–7 are arranged from left to the right on the roof. This setup is designed to monitor any changes in the surface displacement of the roads. Figure 12 presents the results derived from the monitoring process. The data obtained from the monitoring suggest that the deformation process of the surrounding rock can be divided into the following three distinct stages:

Stage I (slow deformation stage): During this stage, the roof experiences minimal deflection and sinking when the stress of the surrounding rock is applied from steps 1 to 6. The maximum subsidence value, located at the middle of the roof, is 16.35 cm, and the rate of deformation is minimal. The side of the roadway undergoes minimal deformation, while the left side experiences a deformation of 2.71 cm.

Stage II (rapid deformation stage): When the surrounding rock's stress is applied from step 6 to step 9, the roof subsidence rate increases rapidly, and the roof subsidence is 36.53 cm. The left side experiences a maximum deformation of 5.84 cm, accompanied by an upward bulging of the floor.

Stage III (rapid deformation stage): The roof experiences its maximum subsidence of 66.00 cm. This occurs when the stress is applied to the surrounding rock transitions from step 9 to step 10. Concurrently, the rate of roof subsidence experiences a significant increase. Both sides undergo severe deformation, with the distortion process accelerating rapidly. The maximum distortion observed on the left side measures 10.12 cm, while the floor exhibits a heave of 51.03 cm.

4.2.4. Analysis of Axial Force Variation of Bolts and Anchor Cables. Three bolt measurement stations, designated as L_1 to L_3, were established on the left side of the roadway to monitor variations in the axial force of bolts. On the right side, three anchor measurement points, denoted as R_1 to R_3, were positioned. The roof was equipped with four bolt measurement points and one anchor cable measurement point. The bolts were labeled as D_1 to D_4 and the anchor

TABLE 2: Physical and mechanical parameters and ratio number of each rock stratum.

| Strata sequence	Lithologic characters	Thickness (m)	The thickness of the model (cm)	Proportion number sand : gypsum : calcium carbonate	Sand quality (kg)	Gypsum quality (kg)	Calcium carbonate (kg)
1	Siltstone	1.00	10.0	8 : 3 : 7	11.94	0.45	1.05
2	Oil shale	5.95	59.5	8 : 3 : 8	11.62	0.42	1.20
3	Siltstone	1.28	12.8	8 : 3 : 7	11.94	0.45	1.05
4	5 #coal	2.12	21.2	(Coal) 20 : 20 : 1 : 5	0.14	0.73	2.94
5	Mudstone	2.00	20.0	8 : 2 : 8	11.94	0.45	1.05
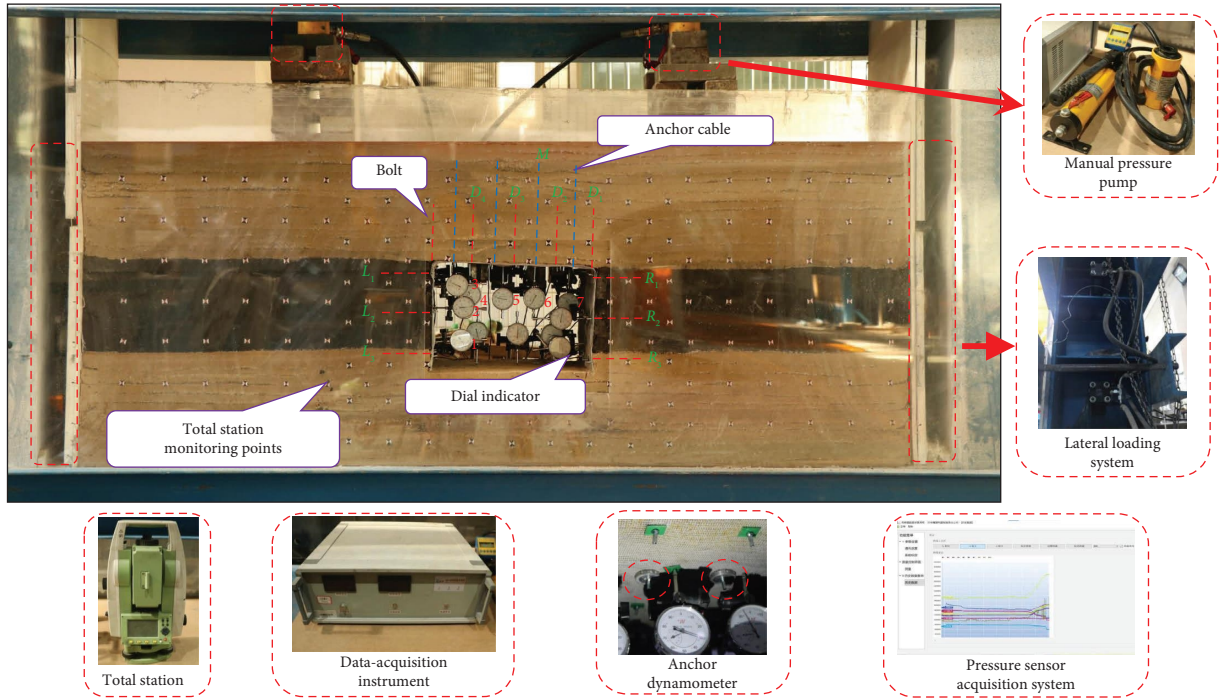
FIGURE 8: Model photos.

TABLE 3: Parameters of bolt and anchor cable.

| Anchor type		Length (m)	Diameter (mm)	Spacing (mm)	Array pitch (mm)	Breaking load (N)
The roof bolt	Prototype	2.40	22.0	900	900	197820
	Model	0.24	2.2	90	90	123.60
The bolt in the sidewall	Prototype	2.20	20.0	1100	900	179836
	Model	0.22	2.0	110	90	112.40
Anchor cable	Prototype	7.20	18.9	900	900	391000
	Model	0.72	1.89	90	90	182.120

TABLE 4: Stepwise loading table of the experimental model.

| Steps	Surrounding rock stress (MPa)	Applied vertical load (kN)	Applied horizontal load (kN)
Step 1	0.63	27.5	3.3
Step 2	1.25	60.3	7.2
Step 3	1.88	93.0	11.2
Step 4	2.50	125.8	15.1
Step 5	3.13	158.6	19.0
Step 6	3.75	191.3	23.0
Step 7	4.38	224.1	26.9
Step 8	5.10	262.1	31.5
Step 9	6.10	314.5	37.7
Step 10	7.70	393.1	47.2

cable was designated as M. The locations of the measurement sites are illustrated in Figure 8, while the monitoring results are presented in Figure 13. Based on the monitoring data, the process of changing the axis force of bolts and anchor cables can be divided into the following three steps:

Stage I: From step 1 to step 6, as the stress on the surrounding rock increases, there is a corresponding gradual increase in the axial force of the bolt. On average, the L_1 and R_1 bolts exhibit an axial force increase rate of 51.2%. Similarly, the L_2 and R_2 bolts show an average axial force growth rate of 58.5%, while the L_3 and R_3 bolts have an average growth rate of 53.9%. Compared to the middle and lower portions, the upper portion of the two sides of the roadway experiences a higher bolt axial force. The roof bolts experience an average axial force growth rate of 44.9%.

Stage II: As illustrated in Figures 13(a) and 13(b), the depth of coal damage in the center and upper sections of the roadway on both sides surpasses the bolt length when the surrounding rock stress is loaded from steps 6 to 9. The failure of the middle and upper bolts on both sides of the roadway leads to a decrease in axial force. Compared to stage I, the axial force of the top bolt has decreased by 23.3%, the center bolt's axial force has reduced by 3.0%, while the axial force of the bottom corner bolt continues to increase. As depicted in
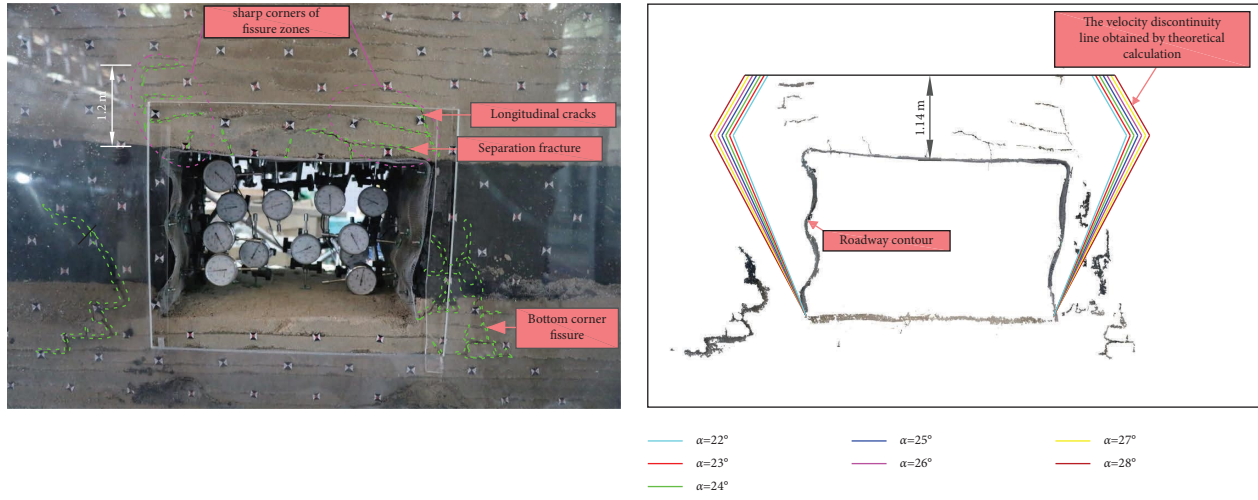
(a)

(b)

FIGURE 9: Fracture distribution (step 6). (a) Model photo. (b) Sketch.
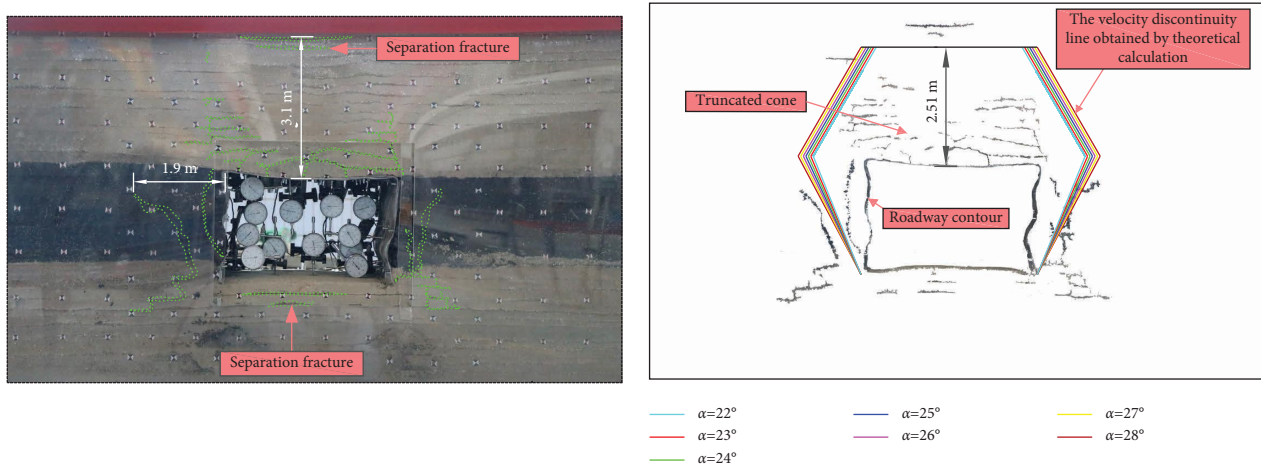
(a)

(b)

FIGURE 10: Fracture distribution (step 9). (a) Model photo. (b) Sketch.
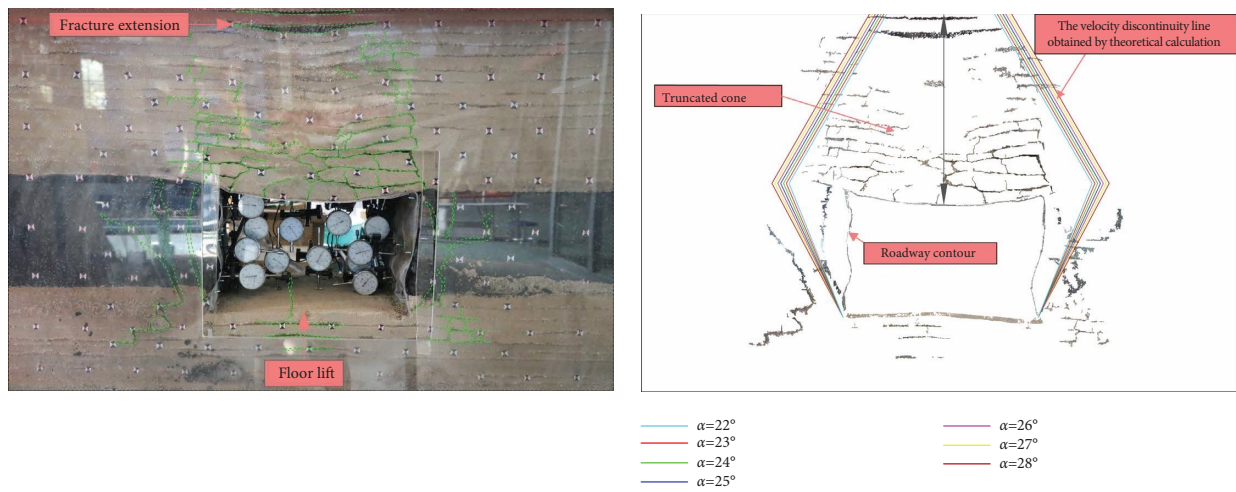
(a)

(b)

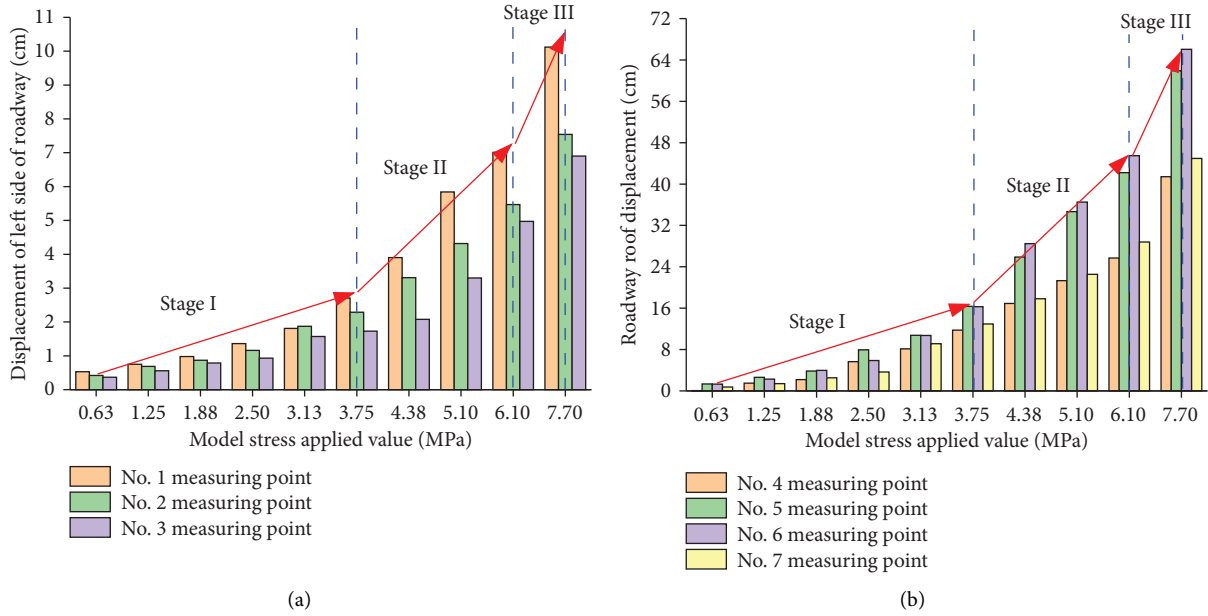FIGURE 11: Fracture distribution (step 10). (a) Model photo. (b) Sketch.

FIGURE 12: Roadway surface displacement changes. (a) Displacement change of the left side of the roadway. (b) Roof displacement change of roadway.

Figure 13(c), the axial force of both the roof bolts and the anchor cables increases. The bolt's average axial force has increased by 19.2% compared to its original value, while the axial force of the anchor cables has risen by 23.1% from its initial value.

Stage III: As depicted in Figures 13(a) and 13(b), the axial force of the middle and upper bolts on both sides persistently decreases as the stress on the surrounding rock is loaded from step 9 to step 10. However, the rate of change is lower in comparison to stage II. In addition, the axial load beneath the sides of the bolts decreases. Figure 13(c) illustrates a rapid decrease in the roof bolt's axial force during the loading process. Compared to stage II, the average axial stress of the bolt experiences a decrease of 8.4%, whereas the average axial stress of the anchor cables initially decreases, then increases by 12.8%.

4.2.5. Cause Analysis of Roadway Surrounding Rock Instability.
Upon conducting a comprehensive analysis of analogous simulations coupled with rigorous field research, it has been determined that the instability of the surrounding rock in the 50213 tailgate can be primarily attributed to the following two predominant factors:

(1) The roadway of the surrounding rock exhibits inferior mechanical properties. The surrounding rock is predominantly fragmented, characterized by numerous internal fissures. The rock layers exhibit low cohesion, making them prone to separation. The presence of water compromises the structural integrity of the overhead oil shale layer.

(2) The design of supporting parameters, which is currently unreasonable, contributes significantly to roof subsidence. The first issue lies in the short length of the anchor cable. Its anchorage section is primarily located within the oil shale layer, a layer known for its low strength. This positioning increases the likelihood of anchor cable failure. The second issue is the low pretightening force of the anchor cable. This low force exacerbates the upward progression of the sharp-angle fracture area. Eventually, this area connects with the separation fracture, leading to the subsidence of the rock strata in the "truncated cone."

5. Roadway Surrounding Rock Stability Control

5.1. Calculation of the Strength of the Rock Support of the Roadway.
By substituting equations (5)–(8) into equation (9), we can derive the upper limit objective function, which is instrumental in calculating the strength of the roadway support.

$$q = f\left(\gamma, \alpha, \varphi_t, \sigma_s, c_t, h_0, h, k, H\right). \tag{13}$$

By using the tailgate of the 50213 panel in Guantun Coal Mine as the engineering background, we can calculate the necessary support strength for different heights of roof damage in the roadway using equation (13). We plotted the variation curves of failure height and supporting strength using MATLAB, as depicted in Figure 14. The parameters used in these calculations are listed in Table 5.

As depicted in Figure 14, a correlation exists between the height of the damaged roadway roof and the required support strength. The required support strength of the roadway increases linearly with the height of the damaged roof. When the failure height of the roadway roof is less than 1.0 m, the necessary roof support strength should exceed 0.55 MPa. The supporting strength of the rib side should be 0.066 MPa.
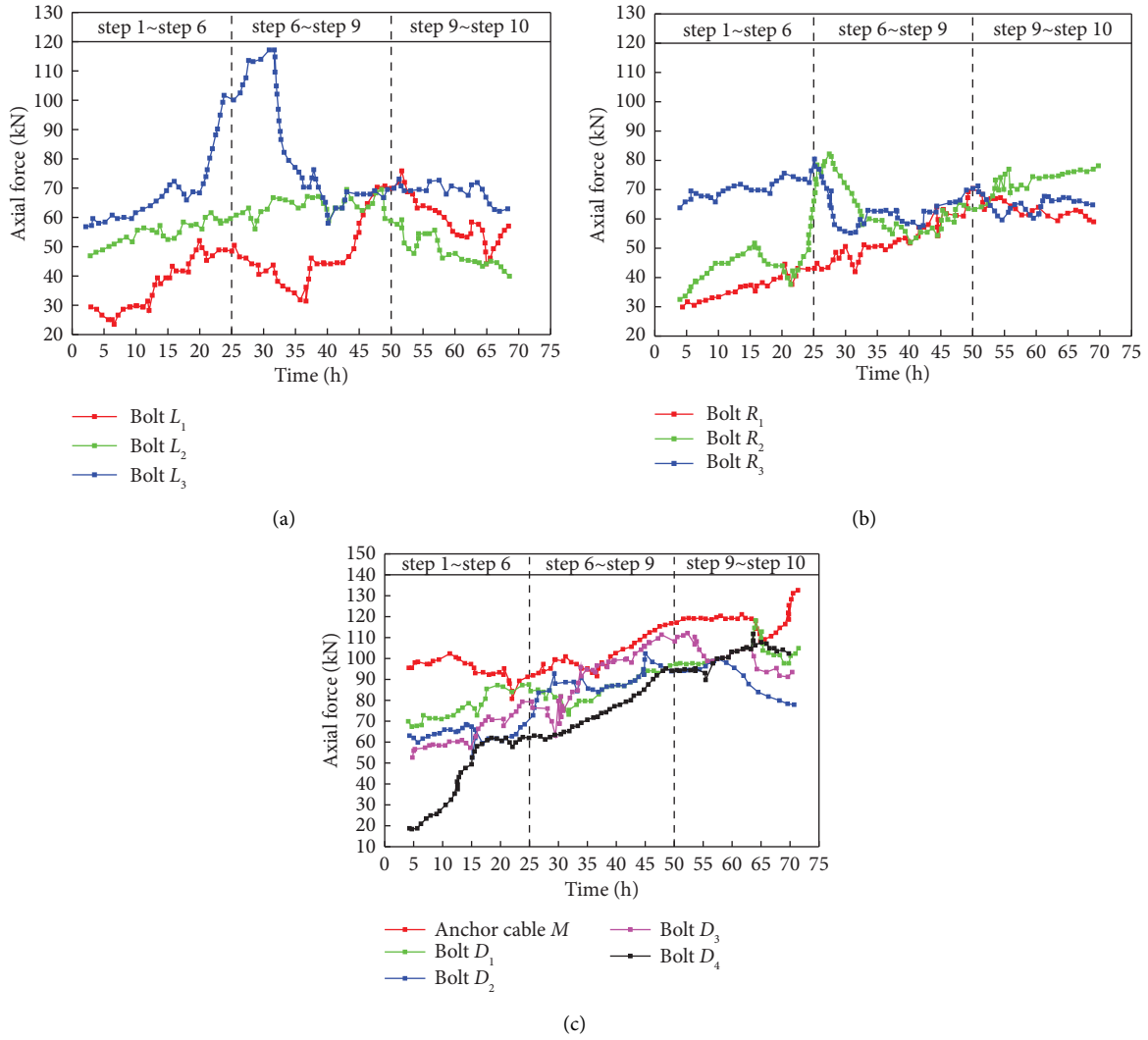
(a)

(b)

(c)

Figure 13: Bolt and anchor cable axial force variation law. (a) The left side of the roadway. (b) The right side of the roadway. (c) The roof of the roadway.
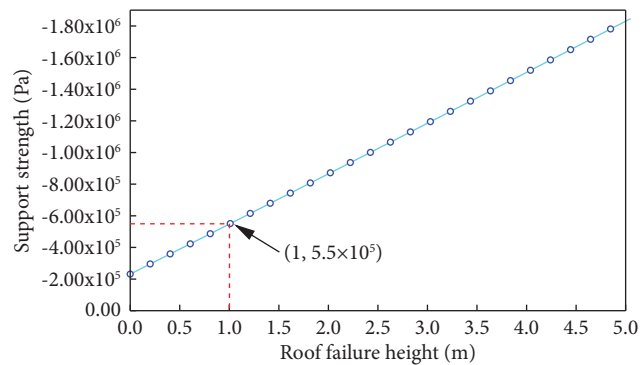

Figure 14: Variation law of supporting strength.

TABLE 5: Parameters required for calculation of support strength.

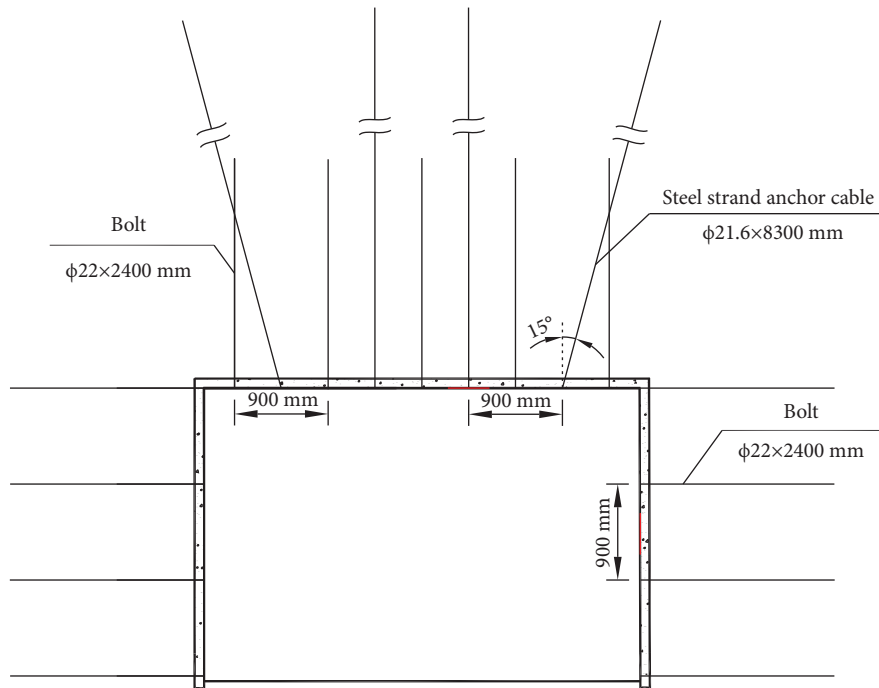| Fracture angle (°)	Internal friction angle (°)	Cohesion (MPa)	Overburden density (N·m^{-3})	Width of the roadway (m)	Height h of the roadway (m)	Pressure coefficient	Overburden rock load (MPa)
28	34	1.08	25470	4.2	2.8	1	7.7

FIGURE 15: Layout of support parameters after optimization.

5.2. Roadway Surrounding Rock Control Scheme. Based on the observed failure mechanism of the "truncated cone" in the roof during physical simulation, we propose to manage the stability of the surrounding rock from four distinct perspectives.

(1) The anchor cables at both corners of the roadway are set at a tilt. The inclined positioning of the anchor cable can expand the scope of the anchorage zone, enhance its shear resistance, and improve the load-bearing capacity of the rock layer at the corners.

(2) The utilization of high prestressing anchor cables on the roof offers two primary advantages. First, it diminishes the shear stress produced at sharp corners in the roadway and hinders the upward expansion of the shear fracture zone at those corners. Second, the high prestress anchor cable effectively compresses the surrounding rock, restricting the deformation of soft oil shale along joint surfaces and averting the formation of primary and secondary cracks upward.

(3) Long anchor cables are used for the roof to avoid having the anchor end in the soft oil shale layer. Moreover, increasing the length of the anchor cables enhances the strength, stiffness, and bearing capacity of the anchorage structure.

(4) The two sides of the roadway exhibit numerous cracks. Consequently, enhancing the diameter, length, and support density of the bolts will improve the stability of the roadway. Figure 15 illustrates the optimal of the roadway support plan. Support parameters are listed in Table 6.

5.3. Simulation Analysis of the Control Effect of the Roadway Surrounding Rock. Using the FLAC^{3D} numerical simulation software, a model with dimensions of 50 m in length, 50 m in width, and 38 m in height has been created. This model is utilized to compare the control effect of the support scheme on the nearby rock before and after optimization. The Mohr–Coulomb criteria are employed in the constitutive relation of the model. The upper boundary of the model is left open, and a uniform stress of 6.80 MPa is applied to represent the weight of the strata above it. In addition, a uniform stress of 6.80 MPa is applied all around. The bottom boundary is constrained with fixed displacement. Table 7 provides a list of the physical and mechanical characteristics of each rock stratum, while Figures 16 and 17 present the simulation findings.

The structural unit in FLAC^{3D} simulates the bolt and anchor cable. The cable component is made of elastic-plastic material, capable of withstanding tensile and compressive stress. Its primary function is to provide local resistance through shear capacity along its length, facilitated by the anchoring agent. The anchor cable structural unit is defined by geometric parameters, material properties, and characteristics of the anchoring agent. The parameters for the bolt and anchor cable are presented in Table 8.

5.3.1. Vertical Displacement. The length and angle of the anchor cable significantly influence the regulation of rock deformation around the roadway following the optimization of support parameters. This results in reduced roof sinking, with the maximum sinking now at 340 mm, representing a 46.7% decrease from preoptimization levels. In addition,

TABLE 6: Support parameters.

Programs	Classification	Diameter (mm)	Length (mm)	Spacing (mm)	Row spacing (mm)	Pretightening force (kN)
Program 1 (original program)	Roof bolt	22.0	2400	900	900	60
	Bolt in sidewall	20.0	2200	1100	900	60
	Anchor cable	18.9	7200	900	900	100
Program 2	Roof bolt	22.0	2400	900	900	80
	Bolt in sidewall	22.0	2400	900	900	80
	Anchor cable	21.6	8300	900	900	120

TABLE 7: Physical and mechanical parameters of rock strata.

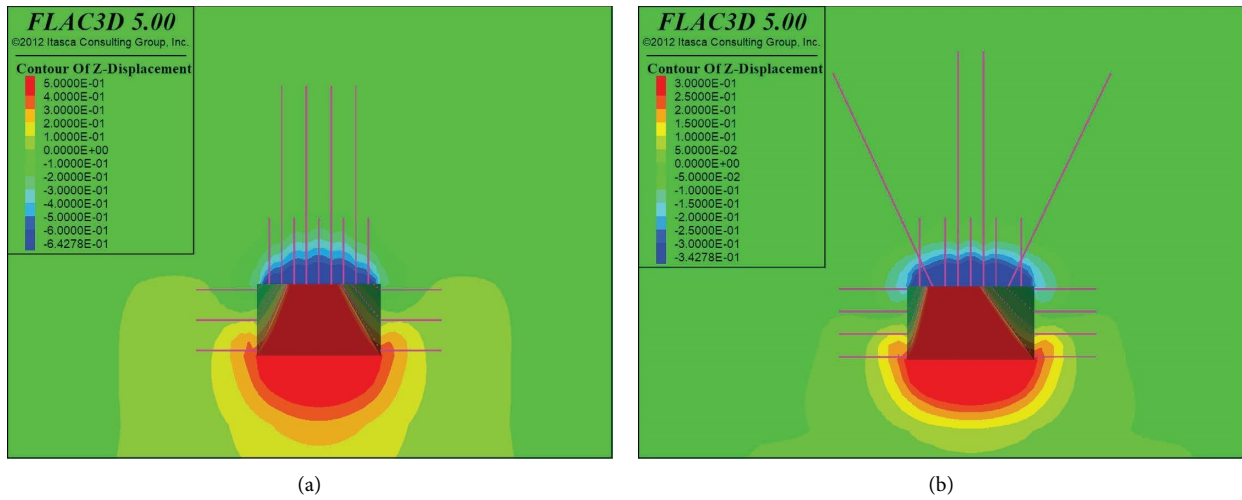| Lithologic characters	Bulk modulus (GPa)	Tensile strength (MPa)	Shear modulus (GPa)	Density (kg/m^3)	The angle of internal friction (°)	The force of cohesion (MPa)
Coal	0.23	1.25	0.33	1430	25	1.20
Fine sandstone	3.56	1.57	1.80	2750	35	1.30
Siltstone	2.56	1.54	0.40	2770	36	1.50
Oil shale	0.26	0.80	1.22	2400	26	0.80
Mudstone	0.16	1.00	0.15	2287	31	1.00

(a)

(b)

FIGURE 16: Vertical displacement cloud diagram of roadway surrounding rock. (a) Program 1. (b) Program 2.
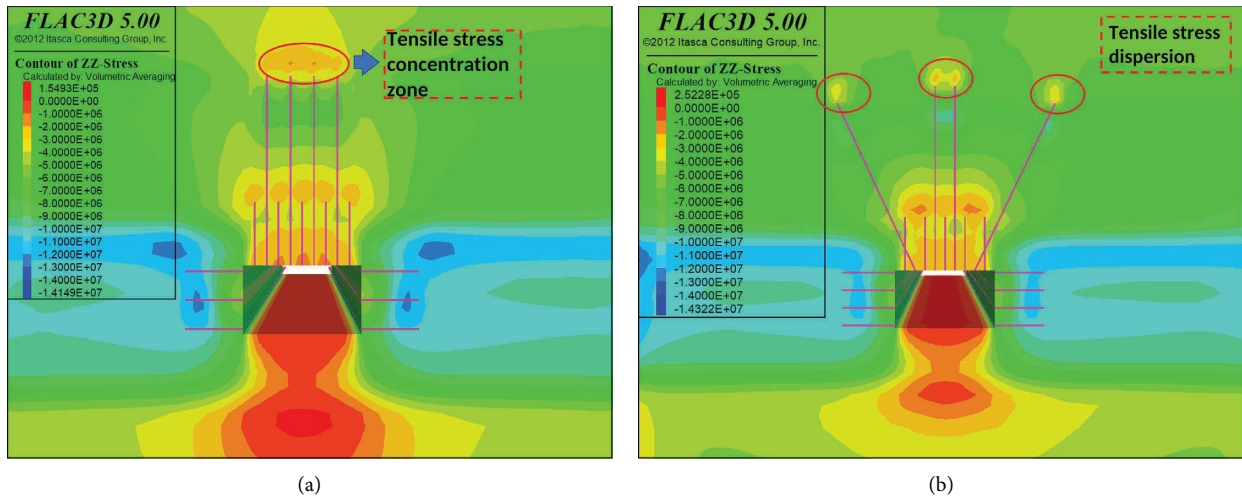

(a)

(b)

FIGURE 17: Vertical stress cloud diagram of roadway surrounding rock. (a) Program 1. (b) Program 2.

TABLE 8: Numerical model support structure parameters.

Programs	Classification	Density (kg/m^3)	Elastic modulus (Pa)	Angle of friction (°)	Cross-section area (m^2)	Anchoring strength (MPa)	Anchoring stiffness (N/m)	Pretightening force (kN)
Programs 1	Bolt	7800	2×10^{10}	25	0.00038	1	2×10^7	100
	Anchor cable	8000	2×10^{11}	30	0.00028	1.6	2×10^8	150
Programs 2	Bolt	7800	2×10^{10}	25	0.00038	1	2×10^7	120
	Anchor cable	8000	2×10^{11}	30	0.00037	1.6	2×10^8	200

there is a 36.2% reduction in horizontal displacement between the two sides. Figure 16 demonstrates the effective control of the roof and surrounding rock sides.

5.3.2. Vertical Stress. The distribution of the vertical stress cloud map showed that, after optimizing the support parameters, the extent of the stress concentration zone and the peak stress on both sides of the roadway decreased. The initial support plan resulted in a significant tensile stress zone at the end of the anchor cable. However, in the second scheme, the tensile stress concentration area is greater as it effectively isolates the tensile stress at the end of the anchor cable, while also reducing the tensile stress on the immediate roof, as shown in Figure 17.

6. Conclusion

(1) Based on a field investigation, it was determined that the axial force of the bolt and anchor cable exceeded the design threshold, leading to a rapid decrease in the axial force of individual bolts and insufficient working resistance. High-density longitudinal cracks were observed at depths ranging from 2.0 to 5.5 m, with additional cracks found on the roadway's side within the range of 1.0–2.2 m.

(2) Based on the upper bound method of limit analysis in plastic mechanics, a roof failure model for soft rock roadways is developed, taking into account factors such as overburden load and support load. By integrating the principle of virtual work and the variational extremum theorem, the upper limit objective function for the roof failure height of soft rock roadways is derived. This function enables the calculation of the upper limit solution for roadway roof failure.

(3) Based on the engineering context of the 50213 tailgate in Guantun Coal Mine, the upper limit objective function calculation formula for roof failure height was used to calculate and verify the roof failure height under varying overlying strata loads through physical simulation. Comparative analysis revealed significant similarities in the evolution and distribution patterns of the two. The physical simulation test uncovered the failure pattern of the surrounding rock in the soft rock roadway. It was observed that the sharp corner of the roadway was initially compromised and extended upwards as the surrounding rock stress increased. Simultaneously, the horizontal separation fracture at the end of the anchor cable and the sharp shear fracture zone became interconnected, leading to the overall instability of the "truncated cone" rock stratum.

(4) The study focuses on the failure mechanism of soft rock mining roadways. It involves optimizing support parameters and proposing the arrangement of high pretightening force long anchor cables in an "inverted trapezoidal" configuration. This proposal is validated by using a numerical model. The findings

indicate a 46.7% reduction in optimized roof subsidence compared to the original scheme, along with a 36.2% decrease in roadway displacement on both sides. The optimized support approach demonstrates effective control over roadway deformation.

Data Availability

The data used to support the findings of this study are included within the article.

Conflicts of Interest

The authors declare that they have no conflicts of interest regarding the publication of this article.

Acknowledgments

References

[1] Q. B. Meng, L. J. Han, W. G. Qiao, G. G. Lin, and J. D. Fan, "Evolution of surrounding rock in pioneering roadway with very weakly cemented strata through monitoring and analysising," *Journal of China Coal Society*, vol. 38, no. 4, pp. 572–579, 2013.

[2] H. P. Kang, "Seventy years development and prospects of strata control technologies for coal mine roadways in China," *Chinese Journal of Rock Mechanics and Engineering*, vol. 40, no. 1, pp. 1–30, 2021.

[3] Q. X. Huang, "Mechanical model for the elastic thick outrigger of roof coal and its application," *Chinese Journal of Rock Mechanics and Engineering*, vol. 17, no. 2, pp. 167–172, 1998.

[4] Y. F. Zeng, Y. P. Wu, X. P. Lai, and C. Wei, "Analysis of roof caving instability mechanism of large-section roadway under complex conditions," *Journal of Mining and Safety Engineering*, vol. 26, no. 4, pp. 423–427+432, 2009.

[5] M. Z. Gao, "Study on bending catastrophe phenomena of anchor roof beam," *Rock and Soil Mechanics*, vol. 25, no. 8, pp. 1267–1270, 2004.

[6] H. Chen, Y. C. Ye, Q. H. Wang, N. Y. Hu, R. Liu, and H. M. Jiang, "Study of direct roof failure form of soft layer in roadway based on rock beam-block theory," *Rock and Soil Mechanics*, vol. 41, no. 4, pp. 1447–1454, 2020.

[7] P. F. Gou, Y. J. Xin, H. Zhang, and Y. M. Shen, "Stability and failure analysis of roof anchors in a deep mine gateway," *Journal of China University of Mining & Technology*, vol. 41, no. 5, pp. 712–718, 2012.

[8] S. W. Liu, R. G. Xu, H. Zhang, X. W. Zheng, S. J. Dong, and W. G. Zhang, "Instability mechanism and classification of lamellate roof with intercalated weak seam in roadway," *Journal of Henan Polytechnic University (Natural Science)*, vol. 29, no. 1, pp. 23–27, 2010.

[9] B. Indraratna, D. A. F. Oliveira, E. T. Brown, and A. P. de Assis, "Effect of soil-infilled joints on the stability of

rock wedges formed in a tunnel roof," *International Journal of Rock Mechanics and Mining Sciences*, vol. 47, no. 5, pp. 739–751, 2010.

[10] Q. Wang, S. C. Li, W. T. Li et al., "Prevention of coal roadway roof accidents based on geological forecast technology," *Journal of Mining & Safety Engineering*, vol. 29, no. 1, pp. 14–20, 2012.

[11] H. S. Jia, W. B. Zhang, S. W. Liu et al., "Failure law and classification control of extremely soft roof in mining roadway of unstable thickness coal seam," *Chinese Journal of Rock Mechanics and Engineering*, vol. 41, no. S2, pp. 3306–3316, 2022.

[12] W. T. Li, Q. Wang, S. C. Li et al., "Deformation and failure mechanism analysis and control of deep roadway with intercalated coal seam in roof," *Journal of China Coal Society*, vol. 39, no. 1, pp. 47–56, 2014.

[13] J. Li, R. G. Zhang, and X. B. Qiang, "The coal pillar width effect of principal stress deflection and plastic zone form of surrounding rock roadway in deep excavation," *Geofluids*, vol. 2022, Article ID 1007222, 17 pages, 2022.

[14] C. J. Hu, C. L. Han, L. X. Wang, B. F. Zhao, and H. Q. Yang, "Cooperative control mechanism of efficient driving and support in deep-buried thick top-coal roadway: a case study," *Energies*, vol. 15, no. 12, p. 4349, 2022.

[15] Y. L. Yang, X. B. Li, and P. F. Li, "Study on surrounding rock deformation mechanism and control of roadway with large section and extra-thick top coal," *Shock and Vibration*, vol. 2021, Article ID 6618424, 11 pages, 2021.

[16] D. D. Chen, X. Ma, Y. Y. Wu et al., "Failure mechanism and divisional differentiated control of surrounding rock in mining roadway under remaining coal pillar in close distance coal seam," *Energy Science & Engineering*, vol. 11, no. 4, pp. 1412–1435, 2023.

[17] C. X. Zhao, Y. M. Li, G. Liu, and X. R. Meng, "Mechanism analysis and control technology of surrounding rock failure in deep soft rock roadway," *Engineering Failure Analysis*, vol. 115, Article ID 104611, 2020.

[18] D. Xu, M. S. Gao, and X. Yu, "Dynamic response characteristics of roadway surrounding rock and the support system and rock burst prevention technology for coal mines," *Energies*, vol. 15, no. 22, p. 8662, 2022.

[19] W. T. Li, X. M. Li, Y. C. Mei, G. Wang, W. D. Yang, and H. T. Wang, "A numerical simulation approach of energy-absorbing anchor bolts for rock engineering," *International Journal of Rock Mechanics and Mining Sciences*, vol. 158, Article ID 105188, 2022.

[20] X. P. Lai, H. C. Xu, P. F. Shan, Y. L. Kang, Z. Y. Wang, and X. Wu, "Research on mechanism and control of floor heave of mining-Influenced roadway in top coal caving working face," *Energies*, vol. 13, no. 2, p. 381, 2020.

[21] M. Fraldi and F. Guarracino, "Analytical solutions for collapse mechanisms in tunnels with arbitrary cross sections," *International Journal of Solids and Structures*, vol. 47, no. 2, pp. 216–223, 2010.

[22] M. Fraldi and F. Guarracino, "Evaluation of impending collapse in circular tunnels by analytical and numerical approaches," *Tunnelling and Underground Space Technology*, vol. 26, no. 4, pp. 507–516, 2011.

[23] X. L. Yang and F. Huang, "Collapse mechanism of shallow tunnel based on nonlinear Hoek-Brown failure criterion," *Tunnelling and Underground Space Technology*, vol. 26, no. 6, pp. 686–691, 2011.

[24] F. Huang and X. L. Yang, "Upper bound limit analysis of collapse shape for circular tunnel subjected to pore pressure based on the Hoek-Brown failure criterion," *Tunnelling and Underground Space Technology*, vol. 26, no. 5, pp. 614–618, 2011.

[25] Q. Wang, H. T. Wang, S. C. Li et al., "Upper bound limit analysis of roof collapse mechanism of large section roadway with thick top coal," *Rock and Soil Mechanics*, vol. 35, no. 5, pp. 795–800, 2014.

[26] X. L. Li, X. Y. Zhang, W. L. Shen et al., "Research on the mechanism and control technology of coal wall sloughing in the ultra-large mining height working face," *International Journal of Environmental Research and Public Health*, vol. 20, no. 1, p. 868, 2023.

[27] S. M. Liu and X. L. Li, "Experimental study on the effect of cold soaking with liquid nitrogen on the coal chemical and microstructural characteristics," *Environmental Science and Pollution Research*, vol. 30, no. 13, pp. 36080–36097, 2022.

[28] S. M. Liu, H. T. Sun, D. M. Zhang et al., "Nuclear magnetic resonance study on the influence of liquid nitrogen cold soaking on the pore structure of different coals," *Physics of Fluids*, vol. 35, no. 1, Article ID 012009, 2023.

[29] S. M. Liu, H. T. Sun, D. M. Zhang et al., "Experimental study of effect of liquid nitrogen cold soaking on coal pore structure and fractal characteristics," *Energy*, vol. 275, no. 7, Article ID 127470, 2023.

[30] L. B. Zhang, W. L. Shen, X. L. Li et al., "Abutment pressure distribution law and support analysis of super large mining height face," *International Journal of Environmental Research and Public Health*, vol. 20, no. 1, p. 227, 2022.

[31] J. C. Zhang, X. L. Li, Q. Z. Qin, Y. B. Wang, and X. Gao, "Study on overlying strata movement patterns and mechanisms in super-large mining height stopes," *Bulletin of Engineering Geology and the Environment*, vol. 82, no. 4, p. 142, 2023.

[32] F. Yang and J. S. Yang, "Limit analysis method for determination of earth pressure on shallow tunnel," *Engineering Mechanics*, vol. 25, no. 7, pp. 179–184, 2008.

[33] X. L. Yang and Z. W. Wang, "Limit analysis of earth pressure on shallow tunnel using nonlinear failure criterion," *Journal of Central South University*, vol. 41, no. 1, pp. 299–302, 2010.

[34] J. Zhang, S. S. Gao, T. Yang, Y. F. He, J. J. Wu, and H. H. Wu, "Study of the failure mechanism of soft rock mining roadways based on Limit Analysis Theory," *Applied Sciences*, vol. 13, Article ID 10323, 2023.

[35] J. Zhang, S. S. Gao, Y. F. He et al., "Study of the roof deformation characteristics of roadway excavation face and unsupported roof distance," *Advances in Civil Engineering*, vol. 2023, Article ID 9916513, 18 pages, 2023.

[36] Y. J. Xu, L. Q. Ma, and N. M. Khan, "Prediction and maintenance of water resources carrying capacity in mining area—a case study in the yu-shen mining area," *Sustainability*, vol. 12, no. 18, p. 7782, 2020.